Predicting Blade Vortex Interaction, Airloads and Acoustics using the Vorticity Transport Model

Mary E. Kelly*, Karthikeyan Duraisamy† and Richard E. Brown‡
Department of Aerospace Engineering
University of Glasgow, Glasgow, G12 8QQ
mkelly@aero.gla.ac.uk, dkarthik@aero.gla.ac.uk, rbrown@aero.gla.ac.uk

ABSTRACT

Interactions between the blades and vortical structures within the wake of a helicopter rotor are a significant source of impulsive loading and noise, particularly in descending flight. Advances in the prediction and understanding of such blade vortex interactions have been aided in recent years by the extensive experimental dataset made available through the HART test programme. Brown's Vorticity Transport Model was used to predict the rotor blade loading, the resultant wake system and the acoustic noise radiation for the HART II rotor. The vorticity conserving properties of the Vorticity Transport Model allow the detailed wake features that are associated with blade vortex interactions to be resolved. The experimental airload data, in particular the higher harmonic loading associated with blade vortex interactions, is matched well by the computations. The computed vorticity distribution in the wake also shows good correlation with the experimentally measured vortex positions. Including a representation of the fuselage within the computation yields marked improvement in the prediction of the vortex positions compared to similar calculations with an isolated rotor. An accoustic analysis, based on a Ffowcs-Williams Hawkings approach, is able to predict accurately the locations of the sound pressure maxima and the upstream attenuation of the sound radiated by the rotor. The principal discrepancies in airload, vortex position and acoustic prediction are confined almost exclusively to the rear of the advancing side of the rotor and, if errors in measuring the blade deflection can be discounted, may be due to minor inaccuracies in modelling the roll-up of the wake.

Nomenclature

a	Speed of sound, m/s
a_{ij}	Coefficients of the interpolation function for each component of the blade deformation
c	Chord, m
C_N	Section normal force coefficient
C_T	Thrust coefficient, $T/\rho A(\Omega R)^2$
M	Mach number
N_a	Number of interpolation functions in the azimuthal direction
N_r	Number of interpolation functions in the radial direction
r	Non-dimensional radial coordinate
R	Rotor radius, m
S	Local vorticity source, s^{-2}
t	Time, s
u	Flow velocity, m/s
u_b	Flow velocity relative to the blade, m/s
X_{hub}	Wake streamwise coordinate, m
Y_{hub}	Wake lateral coordinate, m
Z_{hub}	Wake vertical coordinate, m
y_{el}	Elastic lag motion, mm
z_{el}	Elastic flap motion, mm
μ	Advance ratio
θ_{el}	Elastic blade torsion, degrees
ρ	Density, kgm^{-3}
ω	Vorticity, s^{-1}
ω_b	Bound vorticity, s^{-1}
Ω	Rotor rotational velocity, $rads^{-1}$
ψ	Azimuth angle, degrees

*Postgraduate Research Student
†Lecturer
‡Mechan Chair of Engineering

Presented at the AHS Specialists' Conference on Aeromechanics, San Francisco, CA, Jan. 23-25, 2008.

Introduction

Rotorcraft operate in a highly complex aerodynamic environment which is dominated by the strong vortical structures that are generated by the rotating

blade system. Particularly in descent and in manoeuvring flight, the strong vortices trailed from the tips of the rotor blades are often convected backwards and through the rotor disc. The resultant blade vortex interactions (BVIs) induce impulsive airloads at various positions along the length of the blade, and these loads are associated with an intrusive external noise and often an increase in the vibration of the blades and airframe. Blade vortex interactions thus have a strong impact on the fatigue life of the aircraft as well as on its public acceptance and its environmental footprint. The availability of a reliable tool that can predict accurately the high frequency components of the blade loading, particularly those which result from the wake vortices interacting with the rotor blade, would be of significant benefit to the designers of modern rotorcraft given the current industrial focus on reduction of both maintenance costs and noise level.

Accurate modelling of the wake trailed from the helicopter rotor has thus become one of the primary challenges for the developers of Computational Fluid Dynamics (CFD) methods designed for rotorcraft applications. Accurate prediction of the amplitude and position of the loading perturbations on the rotor that are induced by BVI events relies critically upon the correct simulation of the blade deformation and also the position and strength of the vortical structures within the rotor wake. The complexity of the rotor wake, and the strong mutual dependence of the aerodynamics and structural dynamics, renders accurate prediction of the BVI-related blade airloads a particularly challenging task.

Several wind tunnel experiments and flight tests have been conducted specifically to provide insight into the structure of the rotor wake and its effect on the aerodynamic loading of the rotor blades. In the present context, the most notable of these experiments has been the Higher Harmonic Control Aeroacoustics Rotor Test (HART) programme that was initiated to investigate the influence of blade-vortex interactions on the acoustic signature of helicopter rotors (Refs. 1–4). The release to the public domain of part of the HART II experimental database has provided the developers of rotorcraft CFD tools with a well-defined set of measurements against which the predictions of their models can be verified.

A number of published studies have documented investigations into the performance of numerical methods in predicting BVI-related airloads, and have compared computational predictions against both the HART I and HART II experimental data sets. For example, the computational requirements for accurate prediction of BVI-induced airloads have been investigated extensively by Lim et al. (Ref. 5) and Lim and Strawn (Ref. 6). In their approach, information is cycled between CFD simulations of the rotor aerodynamics and a comprehensive structural analysis code in order to arrive at a stable converged solution. Airload predictions have been compared to the HART II experimental data, and reasonably good agreement has been obtained. Their investigations show, though, that very high grid densities are required to reduce the numerical dissipation of standard CFD techniques to a level where the high frequency character of the BVI-generated airloads can be captured.

As the aerodynamics and structural dynamics of the rotor system are strongly coupled, the sources of discrepancy between experiment and computation can be difficult to determine. There is thus significant merit in performing a decoupled analysis of the structural and aerodynamic behaviour of the system in order to isolate the modelling issues that relate to each independently. Various investigations have used this approach, examples of which include the correlations against UH-60A flight data by Datta et al. (Ref. 7) and Sitaraman et al. (Ref. 8) and the use of prescribed structural dynamics by Lim et al. (Ref. 9) in comparing their aerodynamic predictions to the measured HART I airloads.

In this paper, the aerodynamics of the HART II rotor are modelled using Brown's Vorticity Transport Model (VTM) (Refs. 10 and 11) and results are compared to the HART II experimental data set (Refs. 1–4). The VTM is based on a time-dependent vorticity-velocity formulation of the Navier-Stokes equations, solved computationally on a structured cartesian grid system surrounding the rotor. The method has been designed specifically to reduce numerical dissipation of the vorticity in the flow, thus maintaining the integrity, over many rotor revolutions, of the vortical structures that are present in the rotor wake. This paper aims to confirm that the VTM is well suited to modelling the geometry of the wake to the accuracy and detail that is required for the high frequency components of the blade airload that are associated with BVI to be captured correctly. To decouple the structural dynamic problem from the aerodynamic one, the structural deflection of the rotor blades was prescribed within the computational model. The prescription of the blade dynamics was based on a variable-separable interpolation of the blade deformations that were measured during the HART II experiments (Refs. 1–4).

The HART tests

The Higher Harmonic Control Aeroacoustics Rotor Test was initiated in 1990 as a major international research programme in which researchers from the German DLR, the French ONERA, NASA, and the US Army Aeroflightdynamics Directorate collaborated to

perform two comprehensive wind tunnel tests to investigate the influence of higher-harmonic control in modifying the character of the blade-vortex interactions on a rotor in descending flight, and hence the acoustic signature produced by the system (Refs. 1–4). The tests were conducted at the Large Low-Speed Facility of the German-Dutch Wind-tunnel (DNW) in the 6.0 m by 8.0 m open-jet test section of their anechoic flow facility.

In the first HART programme (Ref. 12), acoustic signature, blade pressures, and blade deformations were measured together with some limited information on the flow velocities within the rotor wake. The wake measurements were made using 3-component Laser Doppler Velocimetry (LDV), but the limitations of this technique in terms of time and spatial field-of-view resulted in measurements being taken at only one azimuthal location on each of the advancing and retreating sides of the rotor. Consequently, very little information was retrieved regarding the structure of the rotor wake or the trajectory of the vortices emanating from the rotating blade system. Given the importance of both vortex trajectory and blade deflection on the resultant BVI-induced airloads and subsequent noise radiation from the rotor, the second HART test concentrated on characterising the rotor wake. By the time of the HART II test, Particle Image Velocimetry (PIV) had matured as a flow measurement technique and was thus employed in place of LDV. Three different flight cases were studied in detail – a baseline (BL) case with conventional control inputs, and two cases with higher harmonic control (HHC) inputs applied to the rotor, the so-called minimum-vibration (MV) and minimum-noise (MN) cases. Acoustic signature, wake geometry, and blade deformation data were measured. Leading edge pressure sensors were positioned at five radial locations between 40% and 97% span, with a more comprehensively instrumented section placed at a radial station of 87%. The sectional airload (C_N) was estimated at this section by integrating the measured pressures. 2048 readings per revolution were taken at every pressure sensor, allowing the high-frequency content of the airload to be resolved without significant aliasing.

HART II test parameters

The model rotor used in the HART II test was based on the properties of the Bo105 main rotor. The rotor had four blades and was scaled both geometrically and aeroelastically to 40% of the full rotor size, giving a radius of 2m and a chord of 0.121m. The rotor blades had a NACA23012 aerofoil with the trailing edge modified to form a 5.4mm (4.46% chord) tab. The blades were rectangular with square tip and incorporated -8° of linear twist and a pre-cone angle of 2.5°.

The rotor was flown at a shaft angle that was designed to simulate descending flight at advance ratio of 0.15 along a 6° glideslope. This test point was selected as being analogous to the full-scale flight condition that yields maximum BVI noise radiation. A small deviation from this nominal descent angle was encountered during the tests. Although some controversy still exists as to the 'true' descent angle at which the experimental data was gathered, all calculations were preformed with the rotor descending at 5.3°. Further operational parameters for the test are summarised in Table 1. A detailed description of the rotor model and the measurement procedures used in the HART II test are given in Refs. 1–4.

Table 1: Rotor operational parameters

Forward velocity	33 m/s
Rotational speed	1041 rpm
Blade passage Frequency	70 Hz
Shaft tilt	5.3°
Thrust coefficient	0.00457
Advance Ratio	0.15

Computational model

The Vorticity Transport Model (VTM), described in detail in Refs. 10 and 11, is a finite volume method based on a vorticity-velocity formulation of the Navier-Stokes equations. Assuming incompressible flow with velocity, u, the associated vorticity distribution $\omega = \nabla \times u$ evolves according to the unsteady vorticity transport equation

$$\frac{\partial}{\partial t}\omega + u \cdot \nabla\omega - \omega \cdot \nabla u = \nu\nabla^2\omega. \qquad (1)$$

In this formulation, the vorticity becomes the fundamental conserved parameter within the flow. The velocity at any point near the rotor is related to the vorticity distribution in the flow by the differential form of the Biot-Savart equation,

$$\nabla^2 u = -\nabla \times \omega. \qquad (2)$$

The rotor and its surroundings are contained within an adaptive cartesian grid in such a way that cells only exist in regions of the computational domain where the vorticity is non-zero. As the vorticity moves to a new location, new cells are created and any cells that no longer contain vorticity are destroyed. In this way the grid structure is free to follow the evolution of the wake, eliminating the requirement for explicit

numerical boundary conditions at the edge of the computational domain and increasing the computational efficiency of the method.

Moreover, a nested grid system allows for fine resolution close to the rotor and then a systematic decrease in resolution with distance from the rotor hub. At each time step, the velocity at the cell faces is obtained from the vorticity distribution using a fast multipole technique to invert Eq. (2). The vorticity transport equation, Eq. (1) is advanced through time using Toro's Weighted Average Flux method (Ref. 13). This method allows control over the local rate of dissipation of the vorticity, ensuring the spatial compactness of the vorticity distribution in the flow around the rotor. The integrity of the wake is thus maintained for the large number of rotor revolutions that need to be captured if all the BVIs on the rotor disc are to be fully resolved.

In the limit of vanishing viscosity the viscous term $\nu\nabla^2\omega$ in Eq. (1) becomes non-zero only on surfaces immersed in the flow, and can therefore be replaced by a local vorticity source, S. The vorticity source (the contribution from fuselages etc, if present, is neglected in the present work) is modelled as the sum of the shed and trailed vorticity from the rotor blades so that

$$S = -\frac{d}{dt}\omega_b + u_b \nabla \cdot \omega_b \tag{3}$$

where ω_b is the bound vorticity on the blades. An extension of the Weissinger-L formulation of lifting-line theory is implemented on a series of discrete panels along the length of the blade to yield the aerodynamic loading and hence ω_b. In this way the loading on the blades feeds directly into the geometry and strength of the rotor wake, and hence via Eqs. (1) and (2) back into the loading on the blades. A variation on Kirchoff's trailing edge separation model is used to model local blade stall, where the length of the stall cell is given as a prescribed function of local angle of attack based on known aerofoil characteristics. The profile drag of the blade is calculated as a separate function of local angle of attack and is then added to the local aerodynamic force that is calculated from the lifting line model. The simulations presented in this paper were performed with 40 aerodynamic stations along the length of each blade and approximately 55 grid cells per rotor radius. These values give a slightly higher resolution of the flow than presented for example in Ref. 10 and were selected so that the details of the wake structure would be resolved sufficiently for the characteristic signatures of individual BVI events to be evident in the rotor loading.

In the current version of the VTM, fuselages or other solid bodies are represented using an unsteady vortex panel method, described in more detail in Ref. 14. The body surface is discretised into a system of panels. Each panel edge is represented as a vortex filament with constant strength – the filaments on each panel thus form a closed loop of vorticity. The velocity at the centroid of any panel is calculated as the sum of the influences from all vortex filaments on the body together with the velocity induced by all the other vorticity within the flow. The loop strengths are set to satisfy a boundary condition of zero penetration simultaneously at the centroids of all panels. Where represented in the simulations described in this paper, the drive housing for the HART II rotor was modelled using 1908 panels. This yields a level of resolution that is comparable to previous simulations using this approach, for example as described in Ref. 14.

Prescription of the blade dynamics

In the HART II tests, the blade deformation was measured using a non-intrusive optical method, called Stereo Pattern Recognition, as described in Refs. 15–17. Reflective markers were attached to both the leading and trailing edges of all four blades at eighteen regular radial stations from 23% span to the blade tip. The positions of the markers were then recorded at 15° intervals of the blade azimuth. The measurements of blade deflection are thus relatively sparse and are available only as a set of values defined at discrete azimuthal and radial positions. No data were taken at the zero azimuth position and there are missing data where the markers could not be viewed because they lay within the shadow of the drive enclosure and the mounting support, or because the markers had peeled off the blades. To allow the computation of the displacement of the blade at any radial or azimuthal location, to interpolate over the gaps in the data and to smooth the noise that is present in the measurements, an analytical description of the blade deflections was generated. This was done by fitting a separate interpolation surface, using the variable-separable form

$$D(r,\psi) = \sum_{i=1}^{N_r}\sum_{j=1}^{N_a} a_{ij} R_i(r) P_j(\psi), \tag{4}$$

to the discrete data for each component D of the deformations of each of the blades. N_r and N_a are respectively the number of radial and azimuthal interpolation functions $R_i(r)$ and $P_j(\psi)$ used to describe the blade deflection. The radial interpolation functions were taken to be polynomials and the azimuthal interpolation functions were taken to be the components of a Fourier series so that

$$R_i(r) = r^{(i-1)} \tag{5}$$

and

$$P_j(\psi) = \begin{array}{cc} \cos\frac{j-1}{2}\psi & \text{if} \quad j \in \{1,3,5,\ldots\} \\ \sin\frac{j}{2}\psi & \text{if} \quad j \in \{2,4,6,\ldots\} \end{array} \qquad (6)$$

The coefficients a_{ij} of the interpolation function were calculated by enforcing a simple least squares fit to the measured data for the blade deformations. The sets of coefficients required to give an approximation to the elastic flap, lag and torsional deformations z_{el}, y_{el} and θ_{el} of the blades for the BL, MN and MV test cases are given in the Appendix.

The raw experimental data for the elastic blade torsion θ_{el} for the baseline case is compared in Fig. 1 to the interpolation that is obtained using six radial coefficients and nine coefficients in the azimuthal direction. The difference between the interpolation and the experimental data set, as shown in part (c) of the figure, is within the stated error bounds on the measurements of $\pm 0.5°$. Similar treatment of the flap and lag deflections of the blades yields interpolation errors that also lie within the stated measurement error bounds of ± 0.5mm.

The sensitivity of the calculations to the number of interpolation functions used to capture the structural deflection of the blades was investigated by comparing the airloads that were predicted when using two different interpolations; one which used four azimuthal harmonics and one which used six azimuthal harmonics (i.e. 9 and 13 interpolation coefficients in the azimuthal direction, respectively). The number of coefficients in the radial direction was kept constant at six. Figure 2 compares the blade loading at the 87% radial station for the BL test case that was obtained using the two different interpolations. Very little change in the predicted airloads is observed when the number of coefficients in the azimuthal direction is increased from 9 to 13, with the largest differences being confined to the higher harmonic component of the loading at the rear of the rotor disc (Fig. 3). Further investigation revealed that the noise that the interpolation process was designed to eliminate increased significantly if the number of azimuthal harmonics included in the interpolation was increased beyond six, with an associated reduction in the quality of predictions.

A prescription of the blade dynamics was also generated using the data synthesis method described by van der Wall in Ref. 18, where reconstruction of the blade dynamics is based on a best fit to the lowest precomputed mode shapes for the structural deformation of the blades. Using this approach, the mode shapes for flap, lag and torsion are first obtained from a finite element method, and then represented in the radial direction using polynomials of up to 7th order. Fourier series for the azimuthal variation of the amplitudes of each of the modes are then determined by enforcing a least squares fit to the experimental data. Figure 4 compares the airload at the 87% radial station of the HART II blade that is predicted by the VTM when using van der Wall's interpolation and when using the variable-separable interpolation described above. The predictions of the lower harmonic content of the loading signal (Fig. 4(b)) are virtually indistinguishable. The largest differences are found at the rear of the rotor disc (ψ =350° to 10°) in the higher harmonic signal

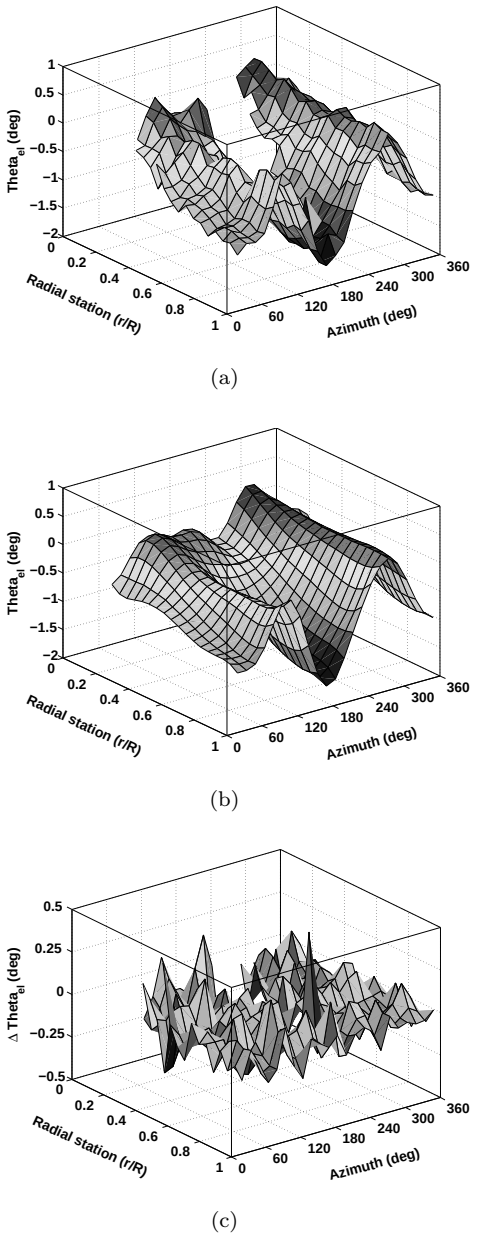

Figure 1: *Elastic blade torsion, (a) Raw experimental data, (b) Variable-separable interpolation ($N_r = 6$ and $N_a = 9$), and (c) The difference between the interpolation and the experimental data.*

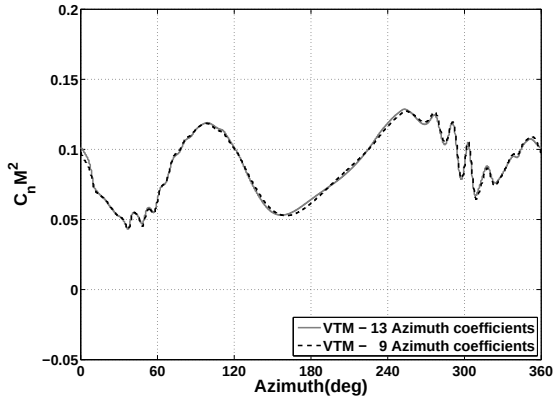

(a) *Full signal*

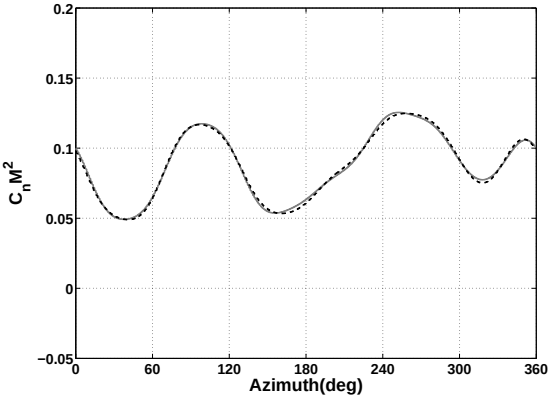

(b) *Signal filtered to include only lower harmonic components (0-10th harmonic)*

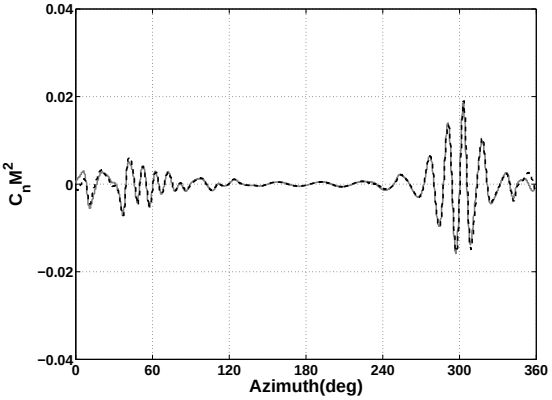

(c) *Signal filtered to include only higher harmonic components (>10th harmonic)*

Figure 2: *Prediction of the blade loading ($C_N M^2$) at 87% span (BL case, with 6 coefficients in the radial direction and varying numbers of coefficients in the azimuthal direction).*

(Fig. 5) – a slight change in the phase of the BVI impulses on the advancing side of the rotor disc is the most noticeable difference between the two sets of results. The similarity between the predictions that are

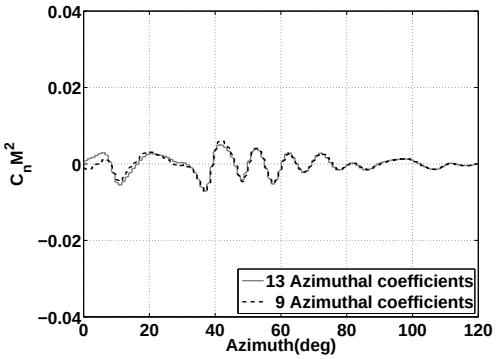

(a) *Advancing side*

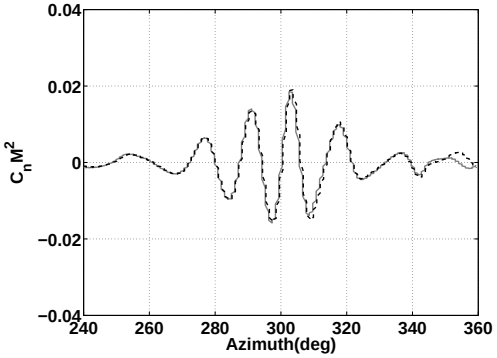

(b) *Retreating side*

Figure 3: *Prediction of the blade loading ($C_N M^2$) at 87% span (BL case, with 6 coefficients in the radial direction and varying numbers of coefficients in the azimuthal direction, signal filtered to include only higher harmonic components (>10th harmonic)).*

obtained using the two different interpolations lends support to the validity of the approach but also suggests that the expense of the modal analysis is not entirely justified in the present context.

Airload prediction

The VTM was used to predict the aerodynamic loading on the HART II rotor for the three test cases for which experimental data was available. Throughout, the structural dynamics of the blades were prescribed using least-squares interpolation on the experimentally measured blade deflections as described earlier. The number of interpolation functions in the radial direction and in the azimuthal direction were six and nine, respectively. The rotor was trimmed to the experimental thrust coefficent and to zero aerodynamic pitch and roll moments about the rotor hub.

Parts (a) of Figs. 6, 10 and 8 show the VTM-predicted blade airload expressed in terms of the non-dimensionalised normal force coefficient $C_N M^2$, at the 87% spanwise location for the BL, MV and MN test

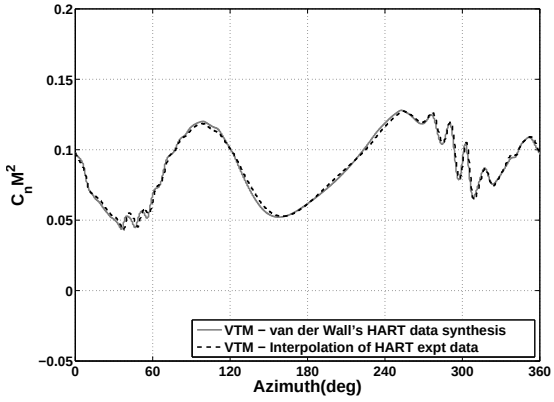

(a) *Full signal*

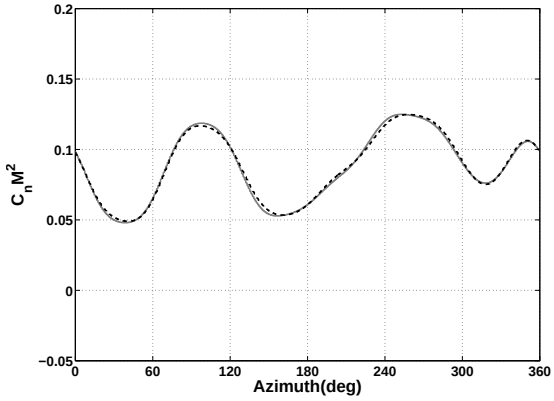

(b) *Signal filtered to include only lower harmonic components (0-10th harmonic)*

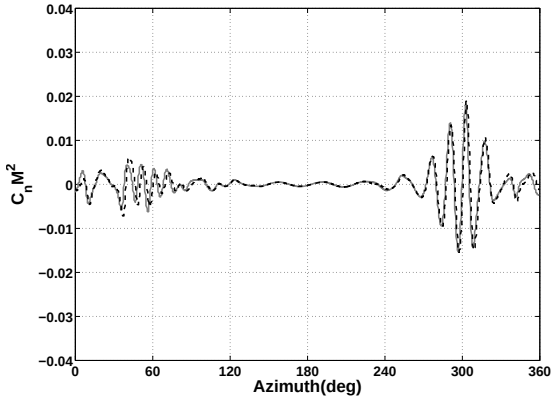

(c) *Signal filtered to include only higher harmonic components (>10th harmonic)*

Figure 4: *Prediction of the blade loading (C_NM^2) at 87% span (BL case, comparison of predictions using van der Wall's synthesised blade deflections (Ref. 18) and variable-separable interpolation on the HART II experimental data).*

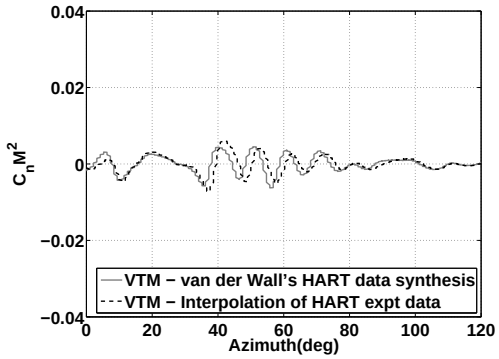

(a) *Advancing side*

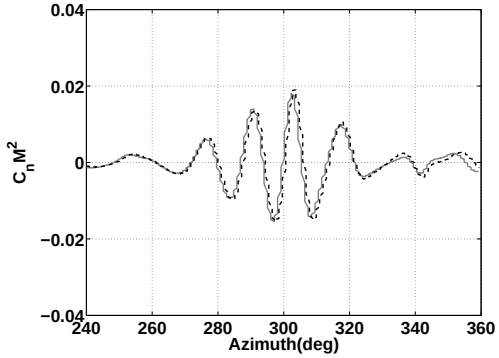

(b) *Retreating side*

Figure 5: *Prediction of the blade loading (C_NM^2) at 87% span (BL case, comparison of predictions using van der Wall's synthesised blade deflections (Ref. 18) and variable-separable interpolation on the HART II experimental data, signal filtered to include only higher harmonic components (>10th harmonic)).*

cases respectively. Parts (b) and (c) of the same figures show the data after filtering at 10/rev to separate the signal into the low-frequency component that is associated primarily with control input and structural deformation of the blades, and the high-frequency component that is almost exclusively associated with the BVI-induced component of the loading. In Figs. 7, 11 and 9, the BVI-induced loading fields on the retreating and advancing sides of the rotor are reproduced with expanded azimuthal scale to aid their interpretation. These figures show the BVI-induced loading on the rotor to be extremely well resolved by the calculations for all test cases. In the BL case, each of the BVI events present in the experimental data for the retreating side of the rotor is captured with the correct position, impulse width and amplitude by the calculations. The MV and MN cases show somewhat greater discrepancy between predictions and experiments, but apart from a rather gross misrepresentation of the amplitude of the furthest-aft BVI in the MV case, the numerical representation of the BVI events on the retreating side of the rotor is generally satisfactory. The BVIs on the advancing side of the rotor disc present a more confusing pic-

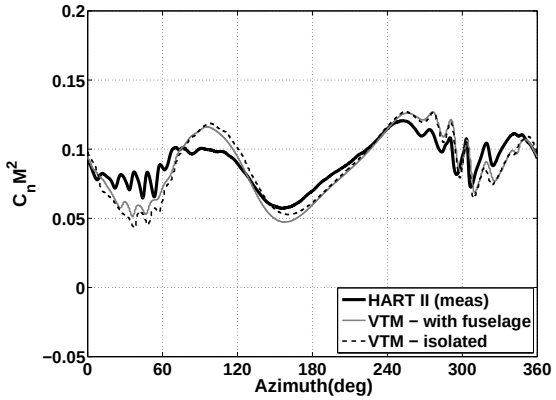

(a) *Full signal*

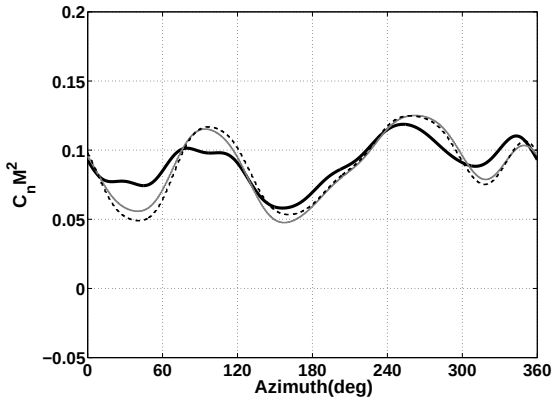

(b) *Signal filtered to include only lower harmonic components (0-10th harmonic)*

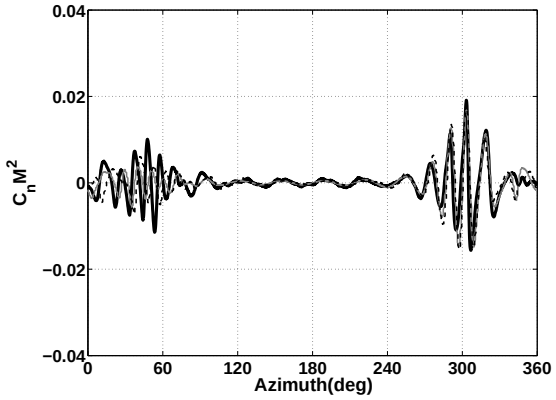

(c) *Signal filtered to include only higher harmonic components (>10th harmonic)*

Figure 6: *Blade loading ($C_N M^2$) at 87% span. BL case.*

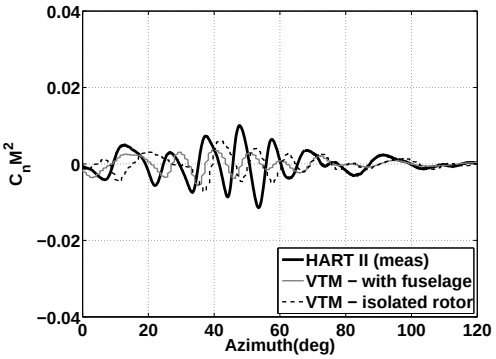

(a) *Advancing side*

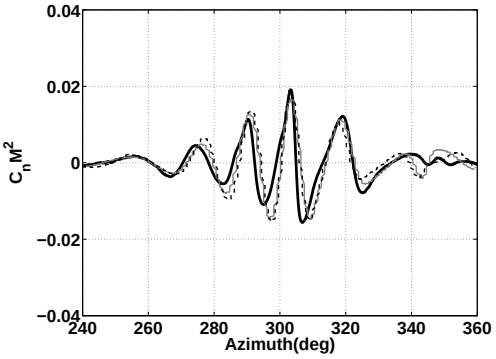

(b) *Retreating side*

Figure 7: *Blade loading ($C_N M^2$) at 87% span. BL case, signal filtered to include only higher harmonic components (>10th harmonic).*

ture. Generally all BVI events that are present in the experimental data are captured by the numerics, but there are errors in the phasing and amplitude of the BVI-induced loading peaks in almost all cases. These deficiencies are consistent with previously documented results (Refs. 3, 5, 19–21) where the amplitude of the BVI events on the advancing side of the rotor disc is often under-predicted and the position and width of the BVI impulses in the airload are less well resolved on the advancing side than those on the retreating side.

Several reasons for the observed discrepancies can be postulated. Incorrect prediction of the strength of the vorticity trailed from the roots of the blades might, for instance, adversely affect predictions of the flow, hence loading, experienced by the blades as they pass near the rear of the disc. No experimental data exists for the wake structure near this part of the rotor disc, but an overly strong root vortex structure could quite feasibly distort the trajectories of the vortices responsible for the BVIs as they pass upwards through the zones of maximum BVI activity on the rotor disc. A parametric study has shown though that the blade loading is relatively insensitive to any variation in the boundary condition that is applied at the root of the blade and hence to the strength of the vortices emanating from there. An additional factor that should be considered is that the loading distribution on the advancing side of the HART II rotor under the exper-

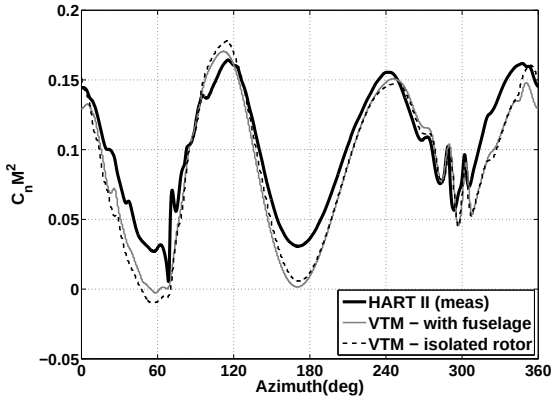

(a) *Full signal*

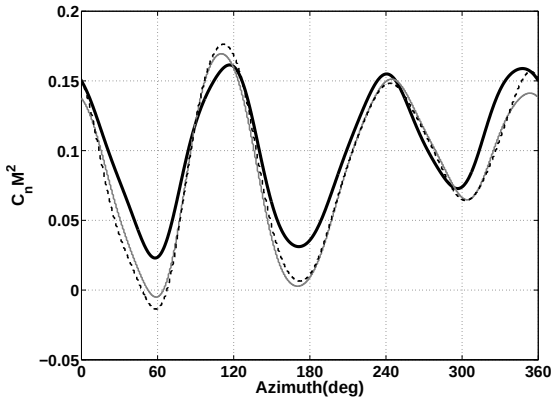

(b) *Signal filtered to include only lower harmonic components (0-10th harmonic)*

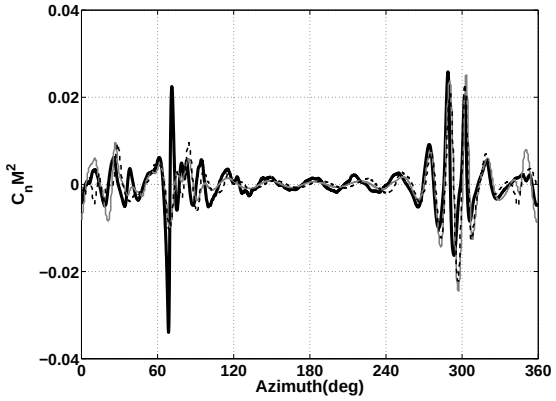

(c) *Signal filtered to include only higher harmonic components (>10th harmonic)*

Figure 8: *Blade loading ($C_N M^2$) at 87% span. MN case.*

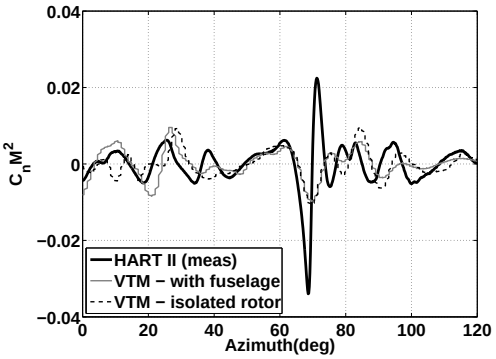

(a) *Advancing side*

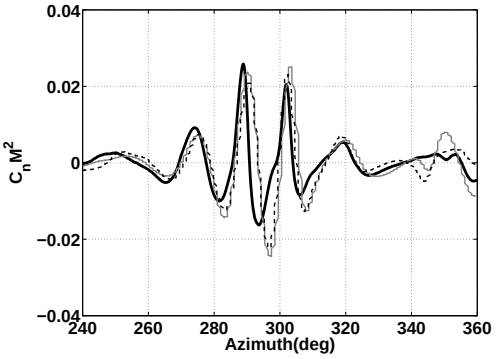

(b) *Retreating side*

Figure 9: *Blade loading ($C_N M^2$) at 87% span. MN case, signal filtered to include only higher harmonic components (>10th harmonic).*

imental conditions is quite unusual in being almost uniformly spread along the length of the blade. This yields a sheet of trailed vorticity behind the blade that is relatively weak and thus that takes some time to roll up to form a coherent tip vortex. The vortical structure of the wake of the HART II rotor is predicted very accurately by the VTM, however, hence the contribution of any inaccuracy in prediction of this roll-up process to the observed errors in blade loading is, at most, very subtle (see the next section of this paper).

Indeed, it is interesting to note though that in all test cases the low-frequency component of the loading is least accurately captured in almost precisely the same sector of the rotor as where the major deficiencies in prediction of the BVI-induced loading are encountered. Given that this component of the loading is primarily affected by control inputs and blade structural deformation, the possibility cannot be excluded at this stage that the discrepancies in both the high- and low-frequency components of the predicted loading on the advancing side of the disc may simply be attributable to errors in the interpolation that was used to prescribe the blade dynamics within the simulation. The missing experimental data for the structural deformation of the blades around 0° and 180° azimuth may have had particularly strong effect on the quality of the structural model on those regions of the advancing side of the rotor that are most strongly influenced by BVI.

The effect on the blade loading of including a repre-

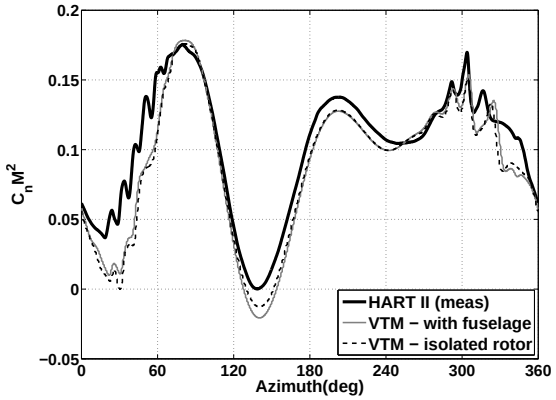

(a) *Full signal*

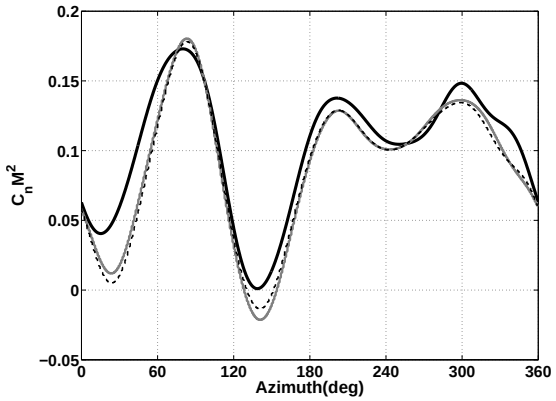

(b) *Signal filtered to include only lower harmonic components (0-10th harmonic)*

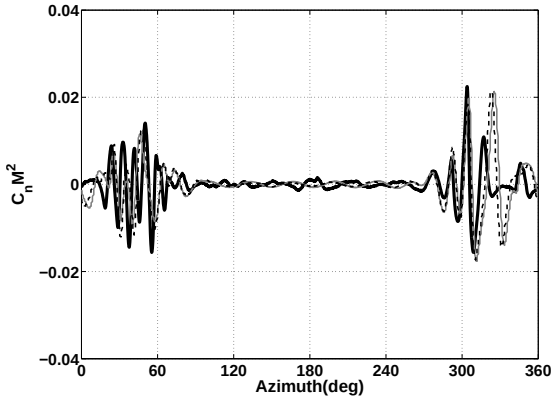

(c) *Signal filtered to include only higher harmonic components (>10th harmonic)*

Figure 10: *Blade loading ($C_N M^2$) at 87% span. MV case.*

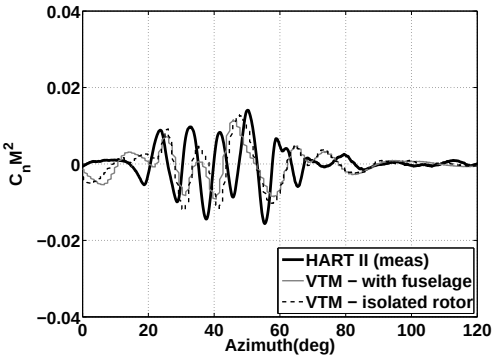

(a) *Advancing side*

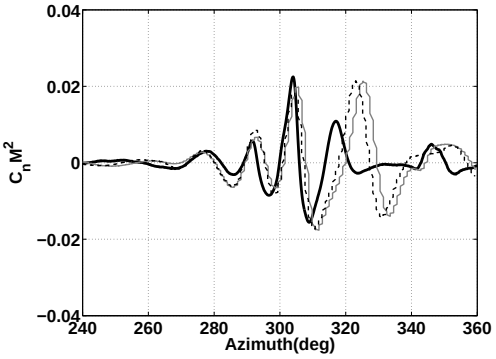

(b) *Retreating side*

Figure 11: *Blade loading ($C_N M^2$) at 87% span. MV case, signal filtered to include only higher harmonic components (>10th harmonic).*

sentation of the rotor drive enclosure within the computations was investigated for all three HART II test cases. The results of simulations with and without the drive enclosure present are compared in Figs. 6, 10 and 8. In all cases the presence of the drive enclosure has minimal effect on the lower harmonic component of the loading. Including a representation of the drive enclosure does, in some cases, reduce to a small extent the phase shift between the experimental data and the computational results for the BVI-induced loading on the advancing side of the rotor disc. The predicted blade loading does thus show a measurable sensitivity to rather subtle changes in the structure of the wake.

Vortex positions

Figure 12 shows the geometry of the wake of the HART II system that is predicted for the BL test case. The wake is visualised by plotting a surface in the flow on which the vorticity has constant magnitude, and the rotor drive enclosure is coloured to show the instantaneous pressure on its surface. The figure illustrates well the characteristic behaviour of the VTM in retaining the spatial compactness of the vortical structures that are present in the flow even after numerous rotor revolutions have elapsed. The relatively strong root-vortex structure, as well as the broad vortex sheet outboard, that is generated behind the blades as they traverse the advancing side of the rotor can be seen clearly. The image also reveals some detail of how this outboard sheet eventually rolls up to

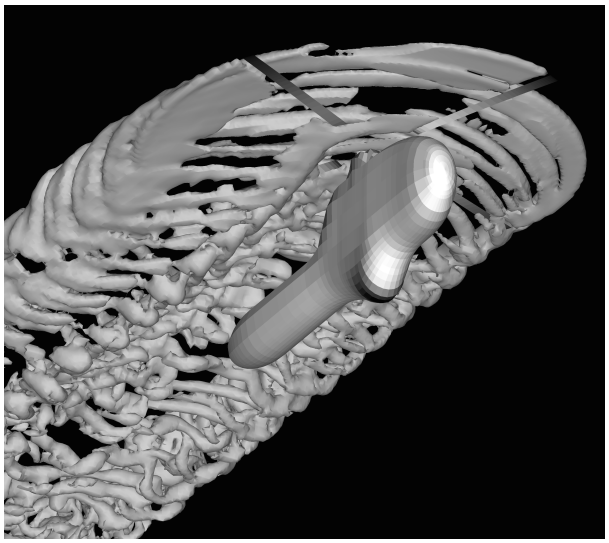

Figure 12: *Visualisation of the VTM-predicted wake geometry (BL case, with representation of the drive enclosure).*

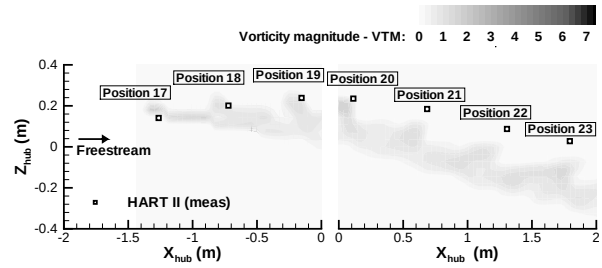

(a) *Advancing side*

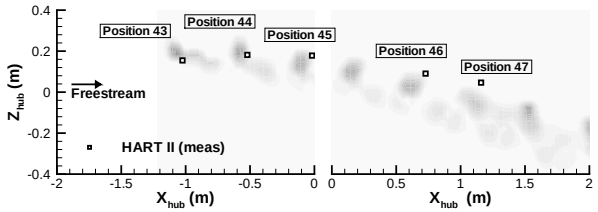

(b) *Retreating side*

Figure 13: *Computed and measured wake structure compared on longitudinal slices through the wake (BL case, isolated rotor, $Y_{hub} = \pm 1.4m$).*

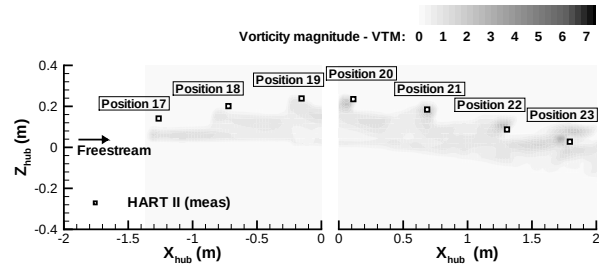

(a) *Advancing side*

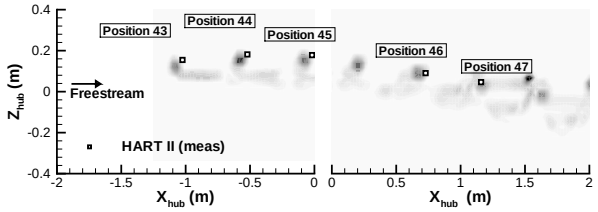

(b) *Retreating side*

Figure 14: *Computed and measured wake structure compared on longitudinal slices through the wake (BL case, with representation of drive enclosure, $Y_{hub} = \pm 1.4m$).*

form a concentrated tip vortex some distance behind the blades.

To illustrate the ability of the model to capture the geometry of the rotor wake, Figs. 13 to 16 show contour plots of vorticity magnitude, as predicted by the VTM, on two longitudinal slices located outboard at 0.7R from the rotor hub, one on the retreating side of the rotor and the other on the advancing side. Measurements of the structure of the rotor wake were gathered during the HART II test using 3-component PIV to extract the velocity field on equivalent slices through the wake of the rotor. To avoid disturbances due to blade presence and the arrangement of the cameras, measurements of the flow structure in the first and third quadrants of the rotor were performed with the rotor at an azimuth of 20°, while similar measurements of the flow in the second and fourth quadrants were made with the rotor at an azimuth of 70°. Time lags in the measurement equipment yield an error of 3.5° in the measured blade azimuth position. These factors have all been accounted for in the presentation of the data. In the Figs. 13 to 16, the experimentally measured positions of the vortex cores are plotted as squares, and are labelled with a position corresponding to the location of the PVI measurement plane. In the hub co-ordinate system Z_{hub} is positive in the upwards direction and X_{hub} is positive aft.

The locations of the maxima in the computed vorticity distribution in the wake show, in general, very good correlation with the experimentally measured vortex positions. Figure 13 shows the vortex positions for the baseline case when an isolated rotor is modelled and Fig. 14 shows those where a representation of the drive housing has been included in the computation. Representing the drive housing in the computations results in an upward deflection of the predicted wake geometry compared to that when the fuselage is ig-

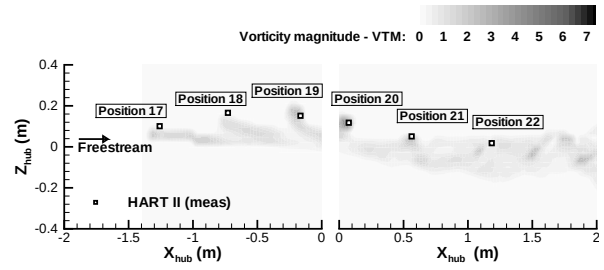

(a) *Advancing side*

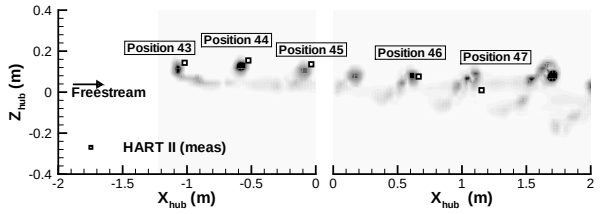

(b) *Retreating side*

Figure 15: *Computed and measured wake structure compared on longitudinal slices through the wake (MN case, with representation of drive enclosure,* $Y_{hub} = \pm 1.4m$*).*

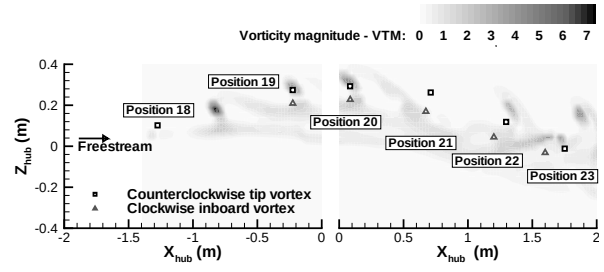

(a) *Advancing side*

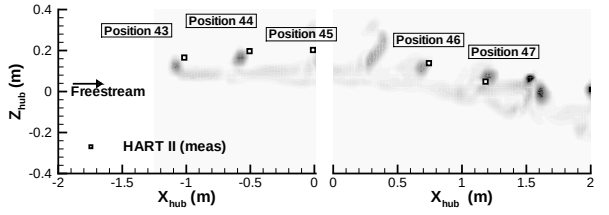

(b) *Retreating side*

Figure 16: *Computed and measured wake structure compared on longitudinal slices through the wake (MV case, with representation of drive enclosure,* $Y_{hub} = \pm 1.4m$*).*

nored, and improves considerably the match between the experimentally-measured and predicted vortex positions.

Figure 15 shows similar vorticity contours for the minimum noise case. The computation included a representation of the drive housing, and, as in the BL case, the locations of predicted maximum vorticity in the flow match very accurately the experimentally measured positions of the vortex cores. On the retreating side of the rotor, the vortices at position 47 and further downstream are perhaps deflected a little too strongly by the distorted flow-field of the drive housing, resulting in vortex cores that lie slightly higher than those measured experimentally. The wake structure of the minimum vibration case, depicted in Fig. 16, is especially interesting. The experimental data shows the existence of a twinned tip-vortex structure on the advancing side of the rotor disc. The existence of this structure was attributed to the reversed loading at the tip of the advancing blade under the conditions of this particular test. The existence of this twin vortex structure is supported by the computational predictions, which show the vorticity distribution on the slice to consist of a sequence of paired vortices, one rotating clockwise and the other counter-clockwise. The positions of both the clockwise and counter-clockwise vortices are in good agreement with the experimental data until position 21 – further aft the counter-clockwise tip vortices lie slightly higher than is observed experimentally. In contrast, the vortex locations at equivalent locations on the retreating side of the rotor are extremely well predicted by the computational method.

A rather revealing consistency is thus observed between the regions of the rotor where the major discrepancies in the predicted BVI-induced airload are encountered and where the prediction of the wake structure is at its least satisfactory. The possible origins of the observed discrepancies have been discussed earlier in this paper – it is sobering to realise though that correlations between predictions and experiment that would be regarded as extremely satisfactory in other contexts appear here to fall short of what is required to capture the BVI-induced component of the blade loading. The results presented here serve to emphasize the extremely demanding requirements on the accuracy of the model of the rotor wake and the structural dynamics of the blades if truly accurate prediction of the BVI-induced airloads on the rotor is to result.

Acoustic analysis

Methodology

The acoustic field that is radiated by the rotor has been computed for all three HART II test cases using a post-processor for the blade aerodynamic loads that implements the Farassat-1A formulation (Ref.

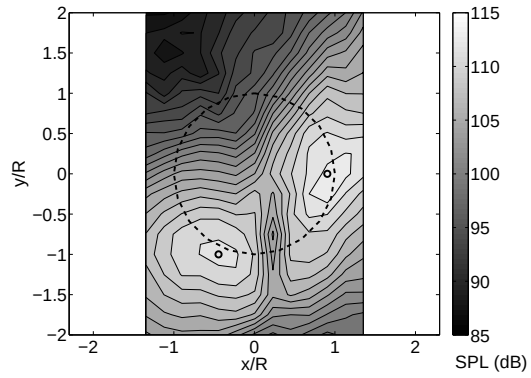

(a) *measured*

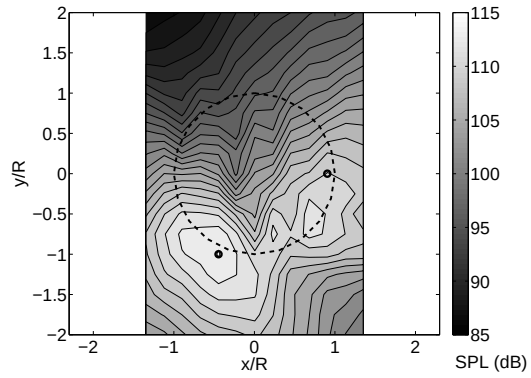

(b) *predicted*

Figure 17: *Predicted and measured SPL noise contours (BL case, rotor position marked by dashed line).*

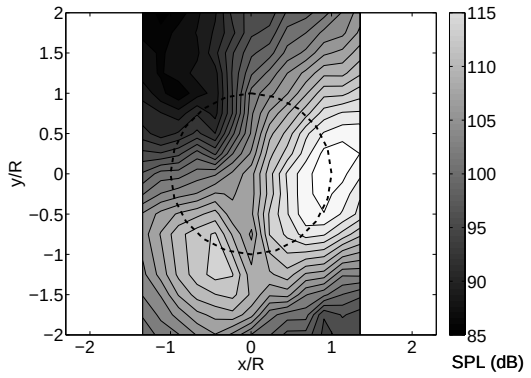

(a) *measured*

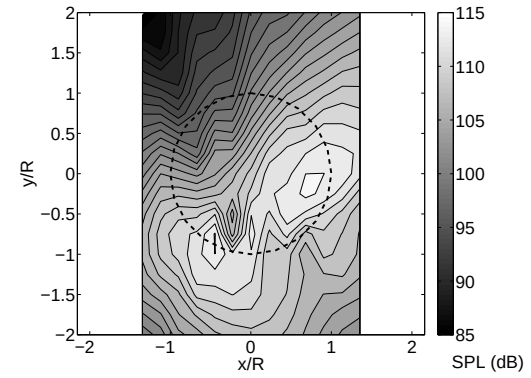

(b) *predicted*

Figure 18: *Predicted and measured SPL noise contours (MV case, rotor position marked by dashed line).*

22) of the Ffowcs Williams-Hawking equations. This formulation is widely used in rotor acoustic calculations because of the efficiency and accuracy that results from its analytic representation of the observer time derivatives. The aerodynamic force contributed by each blade panel is used to construct a point acoustic source at the centre of each panel. Integration of the sound radiated by each of these sources represents the loading noise. The aerodynamic model assumes an infinitesimally thin blade; the thickness noise has thus to be modelled independently. This is done by attaching a source-sink pair to each blade panel. Noise due to quadrupole terms is neglected in the present work. The method that was used to calculate the acoustic field did not account for the effect of the drive enclosure even when it was included in the aerodynamic calculation.

Acoustic predictions

In the HART II experiment, noise measurements were performed with an array of 13 microphones mounted transversally to the axis of the tunnel on a ground plane that was located 2.215m below the rotor hub. A map of the sound intensity on the ground plane was generated by moving this microphone array along the axis of the tunnel. Comparisons between the measured and computed sound pressure level (SPL) on the ground plane for the BL, MN and MV test cases are shown in Figs. 17 - 18. The noise levels are filtered to include only the frequencies between 6-40 times the blade passage frequency, as this is generally accepted to be the range that is dominated by BVI noise.

The presence of the fuselage is responsible for the thin region of reduced noise (Fig. 17(a)) in the centre and to the rear of the rotor disc which is not captured by the numerical method (Fig. 17(b)). The upstream decay in the noise level on the retreating side of the rotor disc in the baseline case is extremely well resolved, however. The location of the SPL maximum on the advancing side is further to the rear of the rotor disc when compared to the experimental result. This is most probably a result of the discrepancy in the predicted phase of the high harmonic components of the blade airload (Fig. 7(a)) compared to the experimental data for the advancing side of the rotor. The magnitude of the SPL maximum on the advancing side of the rotor is slightly under-predicted, which is again

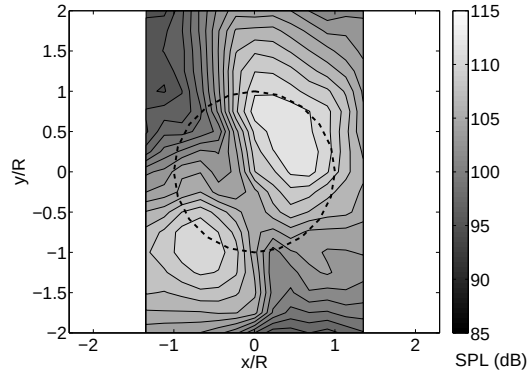

(a) *measured*

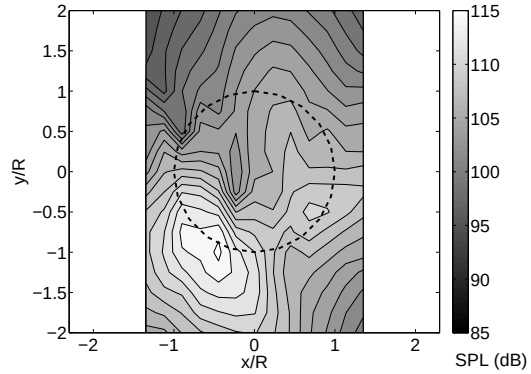

(b) *predicted*

Figure 19: *Predicted and measured SPL noise contours (MN case, rotor position marked by dashed line).*

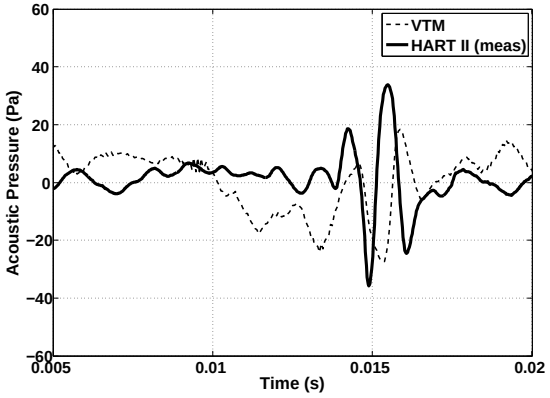

(a) *advancing side microphone*

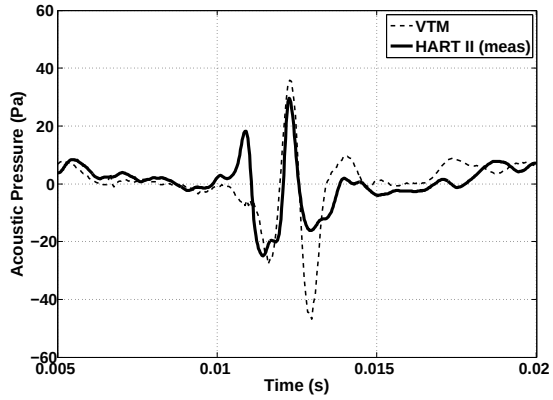

(b) *retreating side microphone*

Figure 20: *Acoustic pressure signal at the SPL maxima on the advancing and retreating side for the Baseline case, each for a single blade passage.*

consistent with the under-prediction of the amplitude of the BVI-related features in the airload between 0 and 90° azimuth. The magnitude and position of the SPL maximum on the retreating side of the rotor is in very good agreement with experiment, however.

For the MV case (Fig. 18) the maximum SPL is higher but the directivity pattern is similar to that in the BL case. The agreement between the experimental measurements and the computations is good, with the SPL maxima on both the advancing and retreating sides of the rotor in the correct position and the maximum on the advancing side being only slightly under-predicted in magnitude. The experimental results show that the maximum SPL is lower in the MN case than in the BL case and that the directivity is shifted towards the front of the rotor. The minimum noise case is the least well predicted of the three cases though, with the maximum SPL on the advancing side of the rotor being under-predicted and the maximum SPL on the retreating side being slightly over-predicted. The position of the maximum on the retreating side is well matched when compared to the experimental data, however. On the advancing side, the SPL maximum is predicted to be slightly aft of the measured position. These discrepancies are again consistent with the errors that are observed in the prediction of the BVI-related airloads for the two test cases.

Contours of sound pressure level do not reveal clearly the noise associated with individual BVI events on the rotor. The predicted and measured time pressure histories for the baseline case are thus plotted in Fig. 20 for the two microphones located at the points of measured maximum noise level on the advancing and retreating sides of the rotor. The positions of these microphones are represented by the small circles in Fig. 17. The computations reproduce the BVI signature at the microphone on the advancing side of the rotor with the correct phase, but the amplitude of several of the peaks is slightly under-predicted. The signal at the microphone on the retreating side of the rotor is also predicted with correct phase. The reason for the rather obviously missing peak in the numerically-generated signal at this location has still

to be determined, however – certainly it is less easily explained in terms of discrepancies in the prediction of the BVI-induced loads than other components of the predicted acoustic signature of the rotor.

Conclusion

Aerodynamic and acoustic predictions using Brown's Vorticity Transport Model (VTM) are compared against the HART II wind tunnel data for an experimental model based on the characteristics of the Bo105 rotor. The version of the code that was used includes a prescription of the blade dynamics that is derived from the HART II experimental data.

Predictions of the geometry of the wake match very closely to experimental data for the positions of the vortex cores on two longitudinal slices through the flow. Incorporating a model of the drive enclosure that was used in the experiments improves markedly the agreement between numerics and experiment. The vorticity conserving properties of the VTM allow the integrity of the vortical structures in the wake to be preserved to well downstream of the rotor. Small discrepancies in the positions of the individual vortices do tend to build up though as the wake convects downstream of the centreline of the rotor, principally on the advancing side of the disc where the rollup of the wake sheet that is created behind the blade is known to be a rather complex process. Nevertheless, elements of this rollup process are well-captured by the VTM, including the formation of a vortex pair type structure from the tip of the advancing blade in the MN test case.

Accurate prediction of the wake geometry translates into very accurate prediction of the higher-harmonic, BVI-induced component of the aerodynamic loading on the blades. Where the wake prediction is the most accurate, generally on the retreating side of the rotor, all BVI events discernible in the experimental data are reproduced by the numerics, usually with the correct phase and often with the correct amplitude. Where the prediction of the wake geometry is poorer, generally on the advancing side of the rotor, the numerical resolution of the BVI-induced loads is less accurate both in amplitude and phase, yet all BVIs seen in the experimental data are still captured. A direct correlation between accuracy of prediction of the wake geometry and accurate resolution of the BVI-induced airloads is obscured to some extent however by the strong coupling that exists between the structural dynamics and the aerodynamics of the blades. Indeed, the coincidence of the regions of least accurate prediction of the low-frequency component of the airload, which is principally influenced by control inputs and blade dynamics, with the regions of the rotor in which deficiencies in the prediction of the BVI-induced airload are also encountered, hints at a small error in the prescription of the blade dynamics as a contributing factor to the observed discrepancies between numerics and experiment.

Similar conclusions extend to the predicted acoustic signature of the rotor. The experimentally-measured directivity of the radiated noise pattern is generally well captured by the numerics, as is the location and magnitude of the maxima in the sound pressure level on the ground plane below the rotor. The upstream decay of the radiated signal is also well-captured, particularly in the BL test case. Yet again the major deficiencies in prediction are encountered on the advancing side of the rotor, where the magnitude and phase errors in the predicted BVI-induced component of the blade loading translate into errors in the position and magnitude of the maxima in the sound pressure field on this side of the rotor.

Thus, although in general the correlation between the predictions of the VTM and experiment is to a standard that would be regarded as satisfactory in other contexts, it also serves to emphasize the extremely demanding requirements on the accuracy of the model of the rotor wake and the structural dynamics of the blades if truly accurate prediction of the BVI-induced airloads on the rotor and hence the acoustic signature of the system is to result. Further work, and possibly further data, is required to isolate the origins of the discrepancies in the results presented here, but it is hoped that the insights presented in this paper will help to encourage the owners of high-quality data sets such as that generated by the HART II programme to continue to share their information more openly with the scientific community.

Acknowledgements

The authors would like to thank Adam Kenyon for his assistance in setting up the model of the drive enclosure for use in the work presented in this paper. They would also like to thank the members of the HART team for their help in producing this study.

References

1. van der Wall, B., Junker, B., Burley, C., Brooks, T., Yu, Y., Tung, C., Raffel, M., Richard, H., Wagner, W., Mercker, E., Pengel, K., Holthusen, H., Beaumier, P., and Delrieux, Y., "The HART II test in the LLF of the DNW - a Major Step towards Rotor Wake Understanding," *Proceedings of the 28th European Rotorcraft Forum*, Bristol, England, 2002.

2. van der Wall, B., Burley, C., Yu, Y., Richard,

H., Pengel, K., and Beaumier, P., "The HART II test - Measurement of helicopter rotor wakes," *Aerospace Science and Technology*, Vol. 8, No. 4, 2004, pp. 273 – 284.

3. Lim, J., Tung, C., Yu, Y., Burley, C., Brooks, T., Boyd, D., van der Wall, B., Schneider, O., Richard, H., Raffel, M., Beaumier, P., Delrieux, Y., Pengel, K., and Mercker, E., "HARTII: Prediction of Blade-Vortex Interaction Loading," *Proceedings of the 29th European Rotorcraft Forum*, Friedrichshafen, Germany, 2003.

4. Yu, Y., Tung, C., van der Wall, B., Pausder, H.-J., Burley, C., Brooks, T., Beaumier, P., Delrieux, Y., Mercker, E., and Pengel, K., "The HART-II Test: Rotor Wakes and Aeroacoustics with Higher-Harmonic Pitch Control (HHC) Inputs - The Joint German/French/Dutch/US Project," *Proceedings of the American Helicopter Society 58th Annual Forum*, Montreal, Canada, 2002.

5. Lim, J., Nygaard, T., Strawn, R., and Potsdam, M., "BVI airloads prediction using CFD/CSD loose coupling," *Proceedings of the American Helicopter Society Annual Forum, Vertical Lift Design Conference*, 2006, pp. 229 – 242.

6. Lim, J. and Strawn, R., "Prediction of HART II Rotor BVI Loading and Wake System Using CFD/CSD Loose Coupling," *Proceedings of the 45th AIAA Aerospace Sciences Meeting and Exhibit*, Paper AIAA-2007-1281, Reno, Nevada, USA, Jan 2007.

7. Datta, A., Sitaraman, J., Chopra, I., and Baeder, J. D., "CFD/CSD Prediction of rotor vibratory loads in high speed flight," *Journal of Aircraft*, Vol. 43, No. 6, 2006, pp. 1698 – 1709.

8. Sitaraman, J., Baeder, J. D., and Chopra, I., "Validation of UH-60A Rotor Blade Aerodynamic Characteristics using CFD," *Proceedings of the American Helicopter Society 59th Annual Forum*, Phoenix, Arizona, USA, 2003.

9. Lim, J., Tung, C., and Yu, Y., "Prediction of blade vortex interaction airloads with higher harmonic pitch controls using the 2GCHAS Comprehensive code," *Journal of Pressure Vessel Technology*, Vol. 123, 2001, pp. 469 – 473.

10. Brown, R. and Line, A., "Efficient High-Resolution Wake Modelling using the Vorticity Transport Model," *AIAA Journal*, Vol. 43, No. 7, 2005.

11. Brown, R., "Rotor Wake Modeling for Flight Dynamic Simulation of Helicopters," *AIAA Journal*, Vol. 38, No. 1, 2000.

12. Kube, R., Splettstoesser, W. R., Wagner, W., Seelhorst, U., Yu, Y. H., Tung, C., Beaumier, P., J. Prieur, G. Rahier, P. S., Boutier, A., Brooks, T. F., Burley, C. L., Boyd, D. D., Mercker, E., and Pengel, K., "HHC aeroacoustic rotor tests in the German-Dutch wind tunnel: Improving physical understanding and prediction codes," *Journal of Pressure Vessel Technology*, Vol. 2, No. 3, 1998, pp. 177 – 190.

13. Toro, E., "A Weighted Average Flux Method for Hyperbolic Conservation Laws," *Proceedings of the Royal Society of London, Series A: Mathematical and Physical Sciences*, Vol. 423, 1989, pp. 401–418.

14. Kenyon, A. and Brown, R., "Wake Dynamics and Rotor - Fuselage Aerodynamic Interactions," *Proceedings of the American Helicopter Society 63rd Annual Forum*, Virginia Beach, USA, 2007.

15. Schneider, O., "Analysis of SPR measurements from HART II," *Aerospace Science and Technology*, Vol. 9, No. 5, 2005, pp. 409 – 420.

16. Schneider, O., van der Wall, B. G., and Pengel, K., "HART II Blade Motion Measured by Stereo Pattern Recognition (SPR)," *Proceedings of the American Helicopter Society 59th Annual Forum*, Phoenix, Arizona, 2003.

17. Pengel, K., Mueller, R. H. G., and van der Wall, B. G., "Stereo Pattern Recognition - the technique for reliable rotor blade deformation and twist measurement," *Proceedings of the American Helicopter Society International Meeting on Advanced Rotorcraft Technology and Life Saving Activities (Heli Japan)*, Tochigi, Utsunomiya, Japan, 2002.

18. van der Wall, B., "Mode identification and data synthesis of HART II blade deflection data," IB 111-2007/28, ftp://HART-II@ftp.dlr.de, 2007.

19. Dietz, M., Kramer, E., and Wagner, S., "Tip vortex conservation on a main rotor in slow descent flight using vortex-adapted Chimera grids," *Proceedings of the AIAA Applied Aerodynamics Conference*, Vol. 3, 2006, pp. 1776 – 1795.

20. Lim, J. and van der Wall, B., "Investigation of the effect of a multiple trailer wake model for descending flights," *Proceedings of the American Helicopter Society 61st Annual Forum*, 2005, pp. 1063 – 1081.

21. Sim, B. and Lim, J., "Blade-vortex Interaction (BVI) noise and airload prediction using loose aerodynamic/structural coupling," *Proceedings of the American Helicopter Society 62nd Annual Forum*, Phoenix, Arizona, USA, 2006.

22. Farassat, F. and Succi, G. P., "A review of propeller discrete frequency noise prediction technology with emphasis on two current methods for time domain calculations," *Journal of Sound and Vibration*, Vol. 71, No. 3, 1980, pp. 399–419.

Appendix: Interpolation coefficients for blade deformations

Elastic torsion motion (θ_{el}) coefficients (degrees, R in metres)

Blade 1

a_{ij}	$j=1$	$j=2$	$j=3$	$j=4$	$j=5$	$j=6$	$j=7$	$j=8$	$j=9$
$i=1$	-0.73	-2.64	2.21	0.96	3.35	0.13	0.82	0.27	1.43
$i=2$	8.99	24.90	-24.17	-10.45	-37.80	-1.89	-5.55	-5.70	-15.66
$i=3$	-34.10	-89.11	88.06	41.23	145.02	10.43	10.58	26.36	62.17
$i=4$	53.50	148.18	-144.24	-73.70	-261.14	-24.05	-2.57	-51.51	-113.89
$i=5$	-40.94	-117.63	111.63	60.89	220.94	24.29	-9.48	47.13	98.47
$i=6$	12.69	36.11	-33.37	-19.02	-71.09	-8.94	6.40	-16.43	-32.50

Blade 2

a_{ij}	$j=1$	$j=2$	$j=3$	$j=4$	$j=5$	$j=6$	$j=7$	$j=8$	$j=9$
$i=1$	-6.74	-0.23	-2.29	-2.39	-8.01	0.98	-1.59	-2.44	-5.02
$i=2$	55.71	2.95	14.32	22.36	54.63	-10.54	10.38	19.21	36.60
$i=3$	-167.25	-12.08	-29.61	-75.72	-140.81	42.16	-21.35	-58.40	-98.45
$i=4$	226.52	18.57	20.72	121.51	164.58	-78.46	11.87	84.20	121.49
$i=5$	-146.92	-11.45	4.14	-93.37	-86.16	67.99	8.48	-56.90	-67.44
$i=6$	37.49	2.07	-7.23	27.50	15.20	-22.19	-7.81	14.34	12.72

Blade 3

a_{ij}	$j=1$	$j=2$	$j=3$	$j=4$	$j=5$	$j=6$	$j=7$	$j=8$	$j=9$
$i=1$	-2.92	1.95	2.04	-0.76	1.87	0.59	-0.94	-0.94	0.23
$i=2$	24.42	-18.21	-17.82	5.54	-27.97	-5.08	11.42	5.47	-6.56
$i=3$	-79.61	63.82	56.20	-12.34	123.56	19.04	-48.77	-10.39	34.68
$i=4$	110.14	-108.57	-80.45	10.47	-244.15	-34.90	93.89	5.88	-72.97
$i=5$	-71.67	88.63	54.00	-2.11	221.07	30.20	-83.20	3.43	68.53
$i=6$	18.50	-27.89	-13.76	-0.89	-74.89	-9.82	27.73	-3.33	-23.98

Blade 4

a_{ij}	$j=1$	$j=2$	$j=3$	$j=4$	$j=5$	$j=6$	$j=7$	$j=8$	$j=9$
$i=1$	-2.47	0.52	-0.77	-2.14	-0.84	1.80	3.27	-0.68	-2.94
$i=2$	24.95	-5.22	6.51	19.65	1.08	-17.87	-32.56	3.55	24.77
$i=3$	-82.97	19.39	-22.74	-68.33	7.05	65.44	118.19	-3.64	-78.92
$i=4$	116.34	-36.13	41.11	113.78	-25.23	-112.63	-201.54	-7.58	120.05
$i=5$	-76.24	31.60	-35.24	-92.29	26.81	92.05	163.73	17.47	-87.51
$i=6$	19.40	-10.42	11.38	29.24	-9.40	-28.85	-51.05	-9.07	24.58

Elastic flap motion (Z_{el}) coefficients (mm, R in metres)

Blade 1

a_{ij}	$j=1$	$j=2$	$j=3$	$j=4$	$j=5$	$j=6$	$j=7$	$j=8$	$j=9$
$i=1$	-3.18	2.41	-3.55	-3.07	-7.92	2.07	-0.89	-3.00	-2.31
$i=2$	34.62	-33.54	35.65	30.41	56.76	-18.58	8.45	24.55	13.78
$i=3$	-150.81	106.42	-137.32	-120.92	-144.56	56.81	-25.63	-76.98	-23.86
$i=4$	284.47	-202.20	241.98	204.12	224.51	-111.88	47.14	113.38	12.13
$i=5$	-263.24	159.02	-192.09	-159.20	-199.29	116.72	-47.49	-79.28	1.66
$i=6$	85.94	-47.70	58.68	47.95	69.05	-43.13	16.41	21.41	-1.66

Blade 2

a_{ij}	$j=1$	$j=2$	$j=3$	$j=4$	$j=5$	$j=6$	$j=7$	$j=8$	$j=9$
$i=1$	2.18	0.81	-6.87	-2.13	-3.33	1.26	-5.42	-3.84	-0.48
$i=2$	-10.91	-16.19	56.99	21.52	10.08	-11.77	46.57	34.05	-5.03
$i=3$	-12.23	44.59	-183.00	-79.21	29.31	35.12	-152.43	-114.53	49.92
$i=4$	34.76	-90.71	296.14	130.92	-89.97	-61.57	255.66	189.62	-121.86
$i=5$	-60.37	61.80	-223.31	-98.94	71.57	57.98	-215.06	-152.81	114.95
$i=6$	24.75	-14.83	65.31	28.80	-20.21	-18.42	68.83	48.42	-37.41

Blade 3

a_{ij}	$j=1$	$j=2$	$j=3$	$j=4$	$j=5$	$j=6$	$j=7$	$j=8$	$j=9$
$i=1$	10.21	2.18	-9.85	-1.60	9.43	-2.24	-8.04	-1.93	7.45
$i=2$	-88.73	-31.31	102.98	16.07	-110.13	25.43	86.87	14.92	-81.66
$i=3$	274.74	100.31	-389.68	-54.72	466.19	-109.33	-339.12	-43.23	330.11
$i=4$	-476.39	-199.57	722.46	90.28	-849.39	198.66	620.02	66.01	-608.77
$i=5$	381.51	162.92	-612.85	-68.23	704.62	-164.29	-533.81	-49.14	519.26
$i=6$	-122.98	-50.49	197.18	20.11	-223.05	54.02	172.20	14.50	-166.69

Blade 4

a_{ij}	$j=1$	$j=2$	$j=3$	$j=4$	$j=5$	$j=6$	$j=7$	$j=8$	$j=9$
$i=1$	2.42	-0.34	-0.83	-3.40	-2.80	1.55	-0.13	-2.63	-0.59
$i=2$	-14.23	-5.89	9.74	34.55	14.22	-14.79	3.13	22.61	-0.24
$i=3$	10.01	6.25	-43.76	-133.13	-0.54	42.15	-19.44	-74.52	17.63
$i=4$	9.56	-25.54	90.29	227.63	-5.75	-77.37	49.12	117.93	-45.96
$i=5$	-40.18	6.70	-69.03	-180.86	-18.48	77.79	-54.53	-89.92	39.28
$i=6$	16.38	3.56	19.41	55.45	13.40	-27.07	19.97	26.91	-10.68

Elastic lag motion (Y_{el}) coefficients (mm, R in metres)

Blade 1

a_{ij}	$j=1$	$j=2$	$j=3$	$j=4$	$j=5$	$j=6$	$j=7$	$j=8$	$j=9$
$i=1$	14.44	-0.04	-5.27	0.63	10.52	-2.07	-5.09	1.17	2.04
$i=2$	-53.83	1.08	29.60	-9.58	-63.46	20.35	43.47	-9.73	0.85
$i=3$	291.23	-6.24	-91.45	34.74	136.58	-73.07	-139.34	29.03	-48.14
$i=4$	-436.55	-0.15	101.76	-57.44	-125.88	119.96	220.14	-42.08	133.87
$i=5$	307.91	5.38	-54.44	44.23	38.97	-90.56	-168.99	27.84	-139.37
$i=6$	-85.75	-2.93	10.67	-12.59	2.10	25.70	49.90	-6.75	50.41

Blade 2

a_{ij}	$j=1$	$j=2$	$j=3$	$j=4$	$j=5$	$j=6$	$j=7$	$j=8$	$j=9$
$i=1$	9.25	-3.65	4.18	-0.24	2.54	-2.63	2.99	0.22	-2.13
$i=2$	-8.32	36.64	-50.04	2.86	-3.00	23.63	-30.54	-7.44	33.95
$i=3$	140.85	-138.99	174.27	1.93	-53.98	-78.00	119.01	22.77	-160.84
$i=4$	-204.01	234.05	-327.82	-10.00	172.90	119.62	-214.08	-26.95	326.36
$i=5$	138.49	-192.99	281.49	7.65	-183.62	-85.70	181.73	8.78	-299.98
$i=6$	-38.36	62.13	-91.36	-1.10	65.47	23.39	-59.14	1.78	102.11

Blade 3

a_{ij}	$j=1$	$j=2$	$j=3$	$j=4$	$j=5$	$j=6$	$j=7$	$j=8$	$j=9$
$i=1$	12.33	-2.80	3.46	0.42	11.09	-1.88	5.54	-0.12	1.92
$i=2$	-49.79	28.39	-61.18	-4.75	-59.23	19.25	-65.55	4.31	2.76
$i=3$	300.46	-111.47	259.41	9.37	112.02	-72.34	278.82	-29.62	-62.90
$i=4$	-453.48	186.25	-539.15	-2.22	-63.77	127.95	-535.05	71.13	175.14
$i=5$	310.53	-151.34	499.70	-9.48	-27.34	-106.37	475.48	-74.58	-185.21
$i=6$	-80.76	47.83	-172.07	6.64	26.88	33.83	-159.47	28.26	67.96

Blade 4

a_{ij}	$j=1$	$j=2$	$j=3$	$j=4$	$j=5$	$j=6$	$j=7$	$j=8$	$j=9$
$i=1$	21.98	-1.41	-6.98	6.29	27.07	-2.84	-4.95	2.24	10.03
$i=2$	-131.73	16.68	44.27	-70.85	-217.85	29.11	32.11	-3.56	-71.96
$i=3$	571.68	-64.99	-118.64	257.58	683.80	-106.85	-80.31	-32.36	207.90
$i=4$	-910.11	103.78	114.07	-449.41	-1056.93	180.08	91.15	119.92	-296.43
$i=5$	679.56	-80.44	-41.51	377.00	806.12	-142.18	-43.47	-145.22	208.64
$i=6$	-196.00	24.19	0.36	-121.84	-242.50	43.18	4.92	59.18	-58.65